Investigation on Temperature Control Based on Cooled Mine Compressed Air for Mine Refuge Chamber with High-temperature Surrounding Rock

Zujing Zhang[a*], Weishuang Guo[a], Xiangkui Gao[b], Hongwei Wu[c], Ruiyong Mao[a**]

[a] College of Civil Engineering, Guizhou Provincial Key Laboratory of Rock and Soil Mechanics and Engineering Safety, Guizhou University, Guiyang, China

b State Key Laboratory for GeoMechanics and Deep Underground Engineering, Xuzhou, Jiangsu 221116, China

[c] School of Physic, Engineering and computer science, University of Hertfordshire, Hatfield, AL10 9AB, United Kingdom

[*]Corresponding author: tel: +86 185 2391 9513 email: zjzhang3@gzu.edu.cn.

[**]Corresponding author: tel: +86 139 8505 6628 email: rymao@gzu.edu.cn.

Abstract: Acceptable temperature is very important for mine refuge chamber (MRC) to ensure the safety of occupants. A novel temperature control scheme combining cold source storage with mine compressed air (MCA) was proposed for MRCs. An experiment was conducted to explore the characteristics of temperature controlling in a MRC via the MCA. Effects of several main factors such as initial surrounding rock temperature (ISRT), ventilation temperature (VT), ventilation rate (VR) and heat rate (HR) on the performance of temperature controlling in the MRC were numerically studied. Results show that: (1) In the MRC, the heat transfer process between the air and walls will reach a dynamic equilibrium within 0.5 h; (2) The ambient temperature in the MRC increases linearly with the square root of time from1 h to 96 h, the gradient increases with VT and HR but decreases with ISRT and VR; (3) Ventilation with rate of 0.3 m^3/min per capita and temperature of 20 °C can meet the temperature control requirements of a MRC located in the sandstone layer with the ISRT of 32.2 °C. An empirical formula for predicting ambient temperature and a ventilation parameter calculation method for meeting the temperature control goal of the MRC are obtained.

Keywords: mine refuge chamber; mine compressed air; ventilation; surrounding rock; heat rate

Nomenclature

a	Coefficient in L expression	T_v	Ventilation temperature, °C
b	Coefficient in L expression	T_{isrt}	Initial surrounding rock temperature, °C
c	Coefficient in L expression	T_{MCA}	Temperature of the MCA, ℃
C_p	Air specific heat capacity, kJ/(kg·k)	T_0	Reference temperature, K
C_1, C_2,	Model parameters	T'	Fluctuating temperature, K
$C_{1\varepsilon}$, $C_{3\varepsilon}$	Model parameters	u	Velocity, m/s
d	Coefficient in L expression	u′	fluctuant velocity, m/s
e	Constant, 2.7182818284	v	Kinematic viscosity, m^2/s
f	Coefficient in L expression	x	Cartesian coordinates direction
g_i	Acceleration component of gravity in the i directions, m/s^2	**Subscripts**	
G	Ventilation rate for MRC, m^3/h	i	Vector direction
G_b	Generation of turbulence kinetic energy due to buoyancy, J/(s m^3)	j	Vector direction
G_k	Generation of turbulence kinetic energy due to the mean velocity gradients, J/(s m^3)	***Greek symbols***	
h	Coefficient in K expression	ρ	Air density, kg/m^3
i	Coefficient in K expression	τ	ventilating time, h
j	Coefficient in K expression	ε	Turbulent energy dissipation, J/(kg·s)
k	turbulent kinetic energy (J/kg)	β	Coefficient of thermal expansion, 1/K
K	Slope, $°C/h^{1/2}$	λ	Air thermal conductivity, W/(m·K)
l	Coefficient in K expression	μ	Dynamic viscosity, Pa·s
L	Intercept, ℃	μ_T	Turbulent viscosity, Pa·s
m	Coefficient in K expression	σ_k	Prandt1 number
n	Coefficient in K expression	σ_ε	Prandt1 number
P	Mean air pressure, Pa	***Acronyms***	
Q	Heat rate Total in MRC, W	EAHE	Earth-air heat exchanger
Q_{cool}	Cool capacity, kJ	HR	Heat rate
S	Modulus of the mean rate-of-strain tensor	ISRT	Initial surrounding rock temperature
t	Time, s	MCA	Mine compressed air
T	Temperature, K	MRC	Mine refuge chamber
T_a	Ambient temperature in the MRC， °C	PCM	Phase change material
$T_{allowed}$	Allowable temperature in MRC, °C	VT	Ventilation temperature
T_{goal}	Goal temperature in MRC, °C	VR	Ventilation rate

1

1 Introduction

Although renewable energy is vigorously explored for most countries, it is difficult to get rid of the dependence on traditional energy sources such as coal, oil and natural gas in short term [1]. In developing countries like China [2] and India [3], coal still dominates the structure of energy. Approximately 45% of the world's coal was produced in China, where over 90% was produced from underground mines [4]. It is known that underground mining is a very dangerous activity accompanied by potential accidents, such as gas explosions, roofs, fires, etc. [5]. Referring to statistics in China, about 90% of coal mine accidents with 10 or more casualties were caused by explosions, water inrush, coal and gas outbursts, and fires [6]. Many cases have proven that most victims, who were poisoned and killed by smoke in coal mine explosions and fires, could have escaped successfully [7]. Mine refuge chambers (MRCs) provide 96 h or more of safe living space for trapped workers awaiting rescue [8, 9], and they need to be reasonably arranged on escape routes of underground mines [10-12]. Fig. 1 shows the interior scenes of different personnel MRCs in different mines, the number of people refers to the rated capacity of the MRC, which is determined in combination with the number of workers in the service area covered by the MRC. Due to the human metabolism and the initial high temperature surrounding rock, occupants in a MRC may face a life-threatening environment with high temperature and high humidity [16, 17].

(a) 50-person MRC

(b) 72-person MRC [13]

(c) 100-person MRC

(d) 200-person MRC[14]

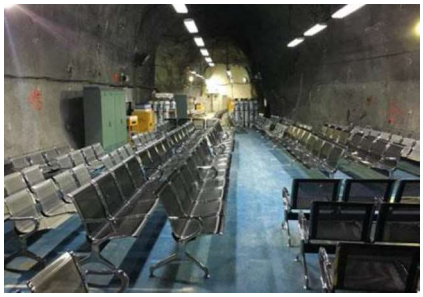

(e) 300-person MRC [15]

Fig. 1. Interior scenes of different personnel MRCs in different mines.

Heat produced by occupants in the MRC ranges from 117 W to 128 W per capita [18]. Moreover, reaction heat of 30 ~ 50 W per capita cannot be ignored, when the CO_2 is absorbed by chemical absorbents [19]. The surrounding rock temperature has an important influence on the temperature control in the underground refuge alternatives. Yantek et.al [20, 21] found that mine air and mine rock temperatures surrounding movable refuge alternatives increased over the 96-h test period. Zhang et al. [22] proved that for a MRC built in sandstone steam, when the initial surrounding rock temperature (ISRT) is not more than 20 °C, the indoor air temperature could be controlled below 35 °C by naturally cooling via the low-temperature surrounding rock. But for MRCs with high ISRT, a comfortable thermal environment means increased the cost of temperature control, because the ventilation rate (VR) via mine compressed air (MCA) may not meet the temperature control requirement [23]. In order to balance the conflicts between the cost of temperature control and the safety of trapped miners, an acceptable temperature should be taken into account against human tolerance within 96 h. In the United States, the apparent temperature of the MRC should not exceed 35 °C [24]. In Indonesia, the allowable values are 32°C WB and 65% RH, respectively [15]. In China, the allowable values are 35°C WB and 85% RH, respectively [25]. Among them, the allowable value in Indonesia is more suitable, according to the studies on the thermal comfort of the underground building environment [26], [27], [28].

Ventilation is a common economic measure for temperature, dehumidification and air quality control for underground buildings [29], [30]. As far as a MRC is concerned, the MCA from a borehole or special pipeline is considered to be the most desirable approach, because it not only has a certain function of temperature control, but also supplies oxygen and dilutes harmful gases [31]. In China, the acceptable minimum VR of the MCA system is 0.1 m^3/min per capita for all underground miners, and the VR of the MCA entering a MRC should not be lower than 0.3 m^3/min per capita [32]. It has been proved that, when the VR is above 0.05 m^3/min per capita, the average CO_2 concentration in the MRC can be controlled within 1% [33]. When the VR is 0.1 m^3/min per capita, the average CO_2 concentration can be controlled at less than 0.5% [32]. When the VR is 0.15 m^3/min per capita, the relative humidity could maintain close to 60% [18]. In fact, on the premise of ensuring the safety of respiratory environment, reducing the use of MCA as much as possible is an important measure to save the operation cost of MRCs [34]. However, for a MRC with an initial high temperature, the amount of air required to maintain a tolerable thermal environment is significantly greater than that required for respiration.

In accidents, temperature control for the high-temperature MRC is very challenging since the reliable power supply used in coal mines is insufficient and electrical equipment needs to be explosion-proof [35]. Nowadays, several cooling technologies based on cold source storage have been developed for MRCs. Wang et al. [36] and Du et al. [37] developed an ice storage air conditioner with an ice storage volume of 5.5 m^3, in which the hot air is pumped via air condensers to the MRC by an explosion-proof fan to obtain cold air. However, the reliability of the ice storage cooling device is low since the capacity of battery used to drive the explosion-proof fan is difficult to guarantee. Encapsulated ice storage plates [38] and ice storage capsule [39] for MRCs were also discussed. Yang et al. [40] developed a liquid CO_2 refrigeration system which transforms liquid CO_2 into gaseous state through decompressing twice to achieve phase change cooling. Yuan et al. [26] proposed a coupled cooling method of latent heat thermal energy storage combined with pre-cooling of envelope for MRCs with high ISRT. In this method, the surrounding rock will be pre-cooled by using cold sources available in the underground in normal times to store a certain amount of cooling and a small amount of PCM in a low-temperature environment. When refuge occurs, the ambient temperature in the MRC can be controlled by the low-temperature rock and PCM. Gao et al. [41-44] systematically studied the temperature control characteristics of the PCM plate and PCM seat used in a 50-person MRC, considering the coupled heat transfer process between surrounding rock, air, and PCM. Yan et al. [45] developed a cryogenic supply system which stores liquid air at -195 °C, as the liquid air is delivered to a heat exchanger, evaporation occurs to provide cooling for MRCs. Compared with other cooling methods, ice storage cooling has a wider range of applications because it is suitable for MRCs with different ISRT. Also, it is the most used cooling technology for practical MRCs, but the current ice storage cooling systems still have a lot of room for improvement in terms of reliability and economy.

Recently, the research on the use of ventialtion as the main temperature control method for MRCs has attracted more attention. Zhang et al. [23] found that when the MRC located in sandstone layer with the ISRT above 27 °C and the ventilation temperature (VT) was equal to the ISRT, the MCA with a VR of 0.3 m^3/min per capita cannot meet the temperature control requirement. Yan et al. [46] tested the temperature control capability of an air-conditioned borehole air supply applied in a 60-person MRC, their test data show that the apparent temperature of the MRC with borehole air supply with cooling was about 9 °F lower than that of the MRC with borehole air supply without cooling. Gao et al. [47] proposed a long vertical earth-air heat exchanger (EAHE) system for MRC temperature control, the system is more suitable for application with a buried depth less than 200 m.

Furthermore, an improved EAHE system by employing backfilling was developed, with the help of the PCM heat storage, the heat transfer rate of airflow in the backfilling system is nearly 1.5 times that of the original system and the suitable for application with a buried depth less than 400 m [48]. In fact, the temperature control performance of a ventilated underground structures is affected by many factors, including the thermal properties of the surrounding rock, the ISRT, the VR and VT, the geometry as well as the inter heat rate (HR), etc. This makes accurate prediction of the heat transfer process of the MRC become extremely difficult. At present, several mathematical models, including a semi-analytical method [26], a Z-transfer coefficient method [49], and a simple heat transfer model [50], etc., have been developed for the heat transfer process of deeply buried ventilated buildings. The establishment of these models is based on a common assumption that the channel cross-section is equivalent to a circle. However, the heat transfer process between the wall and the air around the channel is not uniform in different directions in the short term [22], [23], [51]. Which means that these models are not accurate enough for the 96-hour ventilated MRC.

In conclusion, for a MRC with high ISRT, it is difficult to control the indoor ambient temperature by MCA alone. In this work, a novel temperature control scheme combining MCA and ice storage cooling technology without explosion-proof fan and battery power is proposed for high-temperature MRCs. Considering that heat load forecasting is the prerequisite for this method, the current work mainly focuses on the characteristics of cooled MCA controlling the ambient temperature in MRCs. A ventilation experiment was carried out in laboratory to explore the temperature control characteristics of MRC. Effects of several main factors such as ISRT, VT, VR and HR on temperature control of the MRC were symmetrically investigated by numerical calculations. Based on the numerical results, empirical mathematical methods for predicting the ambient temperature and cooling load in the MRC under the action of cold MCA are respectively obtained, which has good theoretical significance for the further development, configuration and operation of the temperature control scheme for high-temperature MRCs.

2 Model development

2.1 The temperature control system

The novel temperature control system combining the MCA pipeline and cold storage is proposed for high-temperature MRCs to improve the reliability and economy of the temperature control scheme, as illustrated in Fig. 2. The MCA pipeline entering the living room is directly connected to a MCA cooling device, which will cool the MCA before it flows into the breathing environment. It is worth

mentioning here that, to reduce the heat loss during long-distance pipeline transportation, the MCA cooling device is placed in the MRC instead of on the ground. Compared with the existing ice storage cooling technologies for MRC, the obvious significance of the proposed cooling scheme is that it will remove the dependence of the cooling device on the explosion-proof electric fan and the explosion-proof high-power battery, with the assistance of MCA, thereby greatly reducing the system cost and improving the reliability of the cooling system in emergent situations.

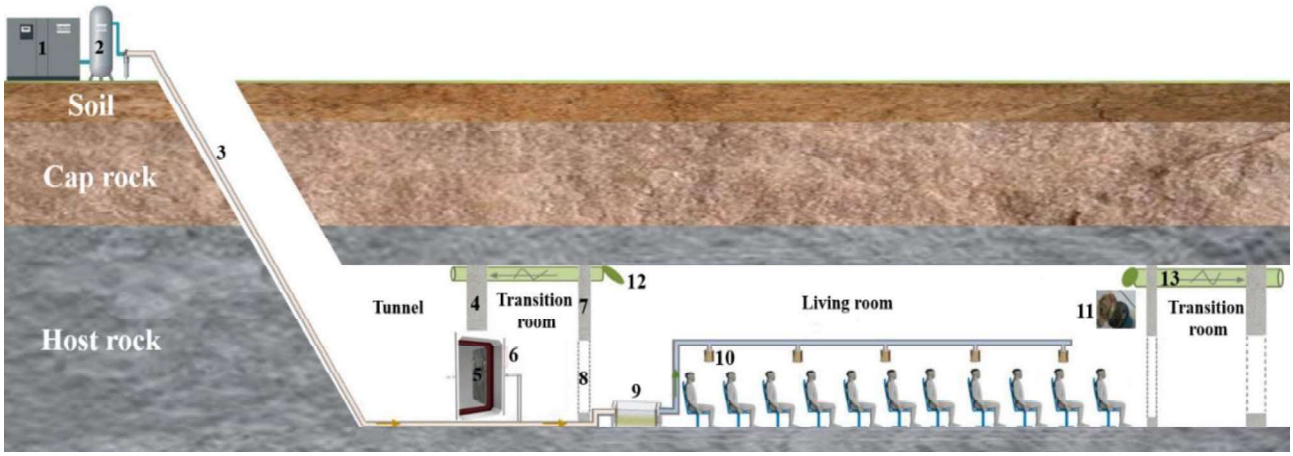

1 - Air compressor, 2 - Air storage tank, 3 - pipeline, 4 - Explosion-protection wall, 5- Protective airtight door, 6 - Air curtain, 7 - Seal wall, 8 - Airtight door, 9 - MCA cooling device, 10 - Silence air inlet, 11 - One-way exhaust valve, 12 - Air outlet, 13 - Exhaust outlet.

Fig. 2. Temperature control system for a high-temperature MRC based on MCA and cooling device.

2.2 Experimental setup

The current work mainly focuses on the temperature control characteristics of the cooled MCA while applied to the high-temperature MRC, instead of the process of the MCA being cooled by the air cooling device. To grasp the characteristics of the ambient temperature changes in the MRC under the action of MCA, as well as to provide reliable data for the validation of the numerical model, an experiment of temperature controlling via MCA for the MRC was carried out. Since the cooling device has not yet been developed, the MCA entering the MRC has not been cooled, but the VT will be affected by the heat exchange behavior during the process of pipeline transmission.

2.2.1 Experimental environment

The experiment was conducted in a MRC laboratory that can accommodate 40 to 60 people, the living room has a size of 20 m in length, 4 m in width and 3 m in height. The wall is made of concrete, the thermal conductivity is 0.81 W/(m·K), the density is 1600 kg/m^3, and the specific heat capacity is 840 J/(kg·K). The fresh air generated by an air compressor (DFB-100A) with a volume flow rate of 11.3 m^3/min first enters an air tank, then will be sent into the living room through vertical and

horizontal alternating pipelines, releasing into the breath environment through 6 silent air inlets distributed on both sides, as presented in Fig. 3. The air inlets were arranged 1.8 m above the ground, with a distance of 3.5 m between two adjacent air inlets. The VR was controlled by a total valve. One-way exhaust valves with a diameter of 110 mm were installed at each end wall of the MRC as air outlets, above the ground 2.4 m. The exhaust valve opened automatically to vent the contaminated air when the relative pressure in the MRC reached 180 Pa. The experiment was conducted on a clear day in September 2021, starting at 8 a.m. Atmospheric temperatures range from 22 to 26 °C during the day and 18 to 22 °C at night.

(a) Test environment (b) Test scenarios

Fig. 3. Test environment and test scenarios.

2.2.2 Experimental principle

Taking into account the air supply capacity of the air compressor, during the experiment, 28 heat lamps with 150 W representing the heat release rate of 35 persons are divided into 4 rows × 7 columns. The row spacing is 1 m and the column spacing is 2 m. All heat lamps are 1 m above the ground. Five temperature measurement points are arranged on three different levels of 0.5 m, 1 m and 1.5 m from the ground. The ambient temperature is monitored by PT100 thermocouple, which is calibrated with 0 □ ice-water mixture. The distance from these measuring points to the near side wall is 1 m. Layout of the heating lamps, air inlets and measuring points is shown in Fig. 4.

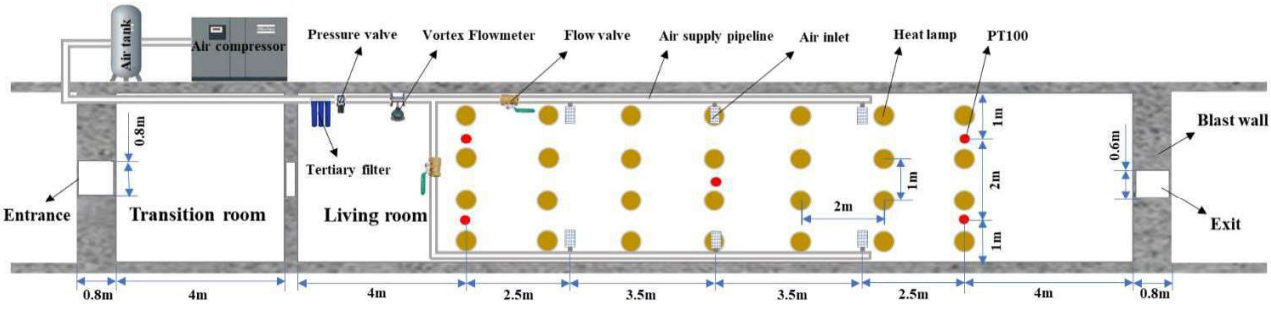

Fig. 4. Layout of the heating lamps, air inlets and measuring points.

The VT at the air inlets is measured by two PT100 thermocouples In addition, during the experiment, the working temperature of the air compressor can be displayed by a built-in temperature monitoring system, and the temperature on the surface of the air tank and the MRC walls can be measured by an infrared thermometer. The ventilation pressure is regulated and determined by a pressure valve, the VR is regulated by a flow valve and determined by a vortex flowmeter.

2.2.3 Experimental procedure

The key steps of the experiment are as follows:

(1) Check the reliability of the system the day before the experiment, make sure that all heating lamps and all temperature sensors can work properly and the data can be automatically recorded.

(2) Prior to heating, two testers enter the MRC laboratory to measure the temperature on the wall surface by using the infrared thermometer. Five measurement points on each wall were taken, and the average initial temperature on the wall surface was determined to be 21.8 °C.

(3) 0.5 h before heating, close all doors and open the temperature monitoring platform to test the initial ambient temperature, which was determined to be 24.5 °C.

(4) Turn on the heating lamps to rise the indoor ambient temperature.

(5) Turn on the air compressor while the ambient temperature rises to about 30 °C, then adjust the ventilation pressure to 0.3 MPa and the VR to 300 m^3/h for 1.67 h.

(6) Adjust the VR to 450 m^3/h for 1 h.

(7) End the experiment and save the experimental data.

2.3 Computational details

2.3.1 Computational domain and mesh

CFD simulations have become a useful tool to calculate heat transfer between the human body and ambient environment [52-54]. The geometric structure of the numerical model refers to the internal structure of the above MRC laboratory. The internal size is 20 m long, 4 m wide and 3 m high. The space of the transition room can be neglected since the heat transfer process mainly occurs in the living room during evacuation. It has been proved that the range of the surrounding rock affected by the heat transfer process within 96 h was 2~2.2 m [23], therefore the wall thickness in the current model was 2.5 m. The occupied area of each person in the MRC should not be less than 1 m^2. The capacity of this model was 50 people considering the typical situation of underground mines. Fifty mannequins with a surface area of 2 m^2 were divided into 4 rows in the living room, the space

occupied by these mannequins can be ignored. Each of the two long sides has five air inlets with a diameter of 0.075 m, and the distance between the two adjacent air inlets is 3.5 m. An air outlet with a diameter of 0.3 m was arranged on each end, as demonstrated in Fig. 5. Boundary types of air inlets, air outlets and mannequin surfaces are defined as velocity-inlet, outflow, and heat-flux wall, respectively.

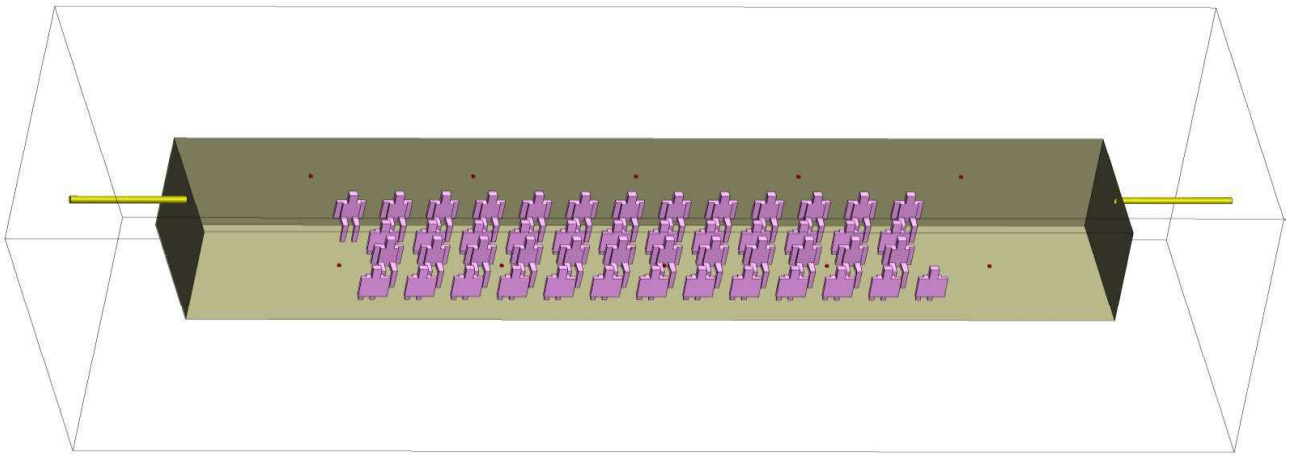

Fig. 5. Geometry of the 50-person MRC numerical model.

Unstructured mesh was adopted for the numerical model by ANSYS ICEM. To minimize the error caused by the mesh quality of the numerical model, the grid independence study is carried out by using five different grids, i.e., 0.97, 1.56, 2.13, 3.15 and 4.14 million cells, respectively. Considering that the following validation of the numerical model involves natural convection and ventilation, the ambient temperature in the MRC at 1 h under natural convection and at 10 h under ventilation are compared for these different numerical grids. As shown in Fig. 6, it can be found that when the number of grids in the numerical model reaches 2.13 million, the ambient temperature in the two different states almost does not change

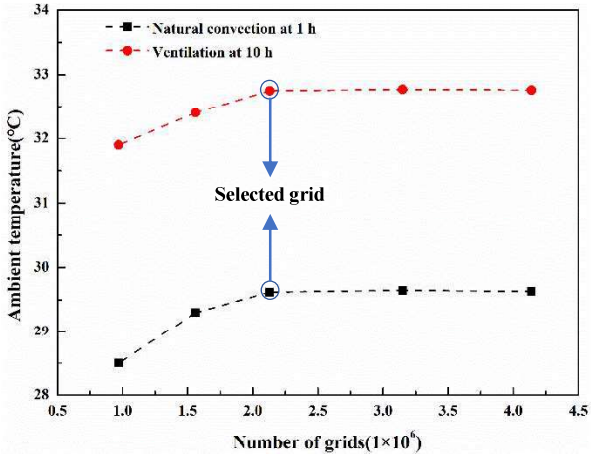

Fig. 6. Comparisons of numerical results with five different grids under two different conditions

For the sake of computing resource economics, the numerical grid with 2.13 × 10^6 cells is

selected, see in Fig. 7. Grid cells on surfaces of mannequins, coupling wall, air inlets and air outlets were encrypted separately to improve the mesh quality. The minimum orthogonal quality of the mesh was 0.37, with a minimum angle of 18.6°.

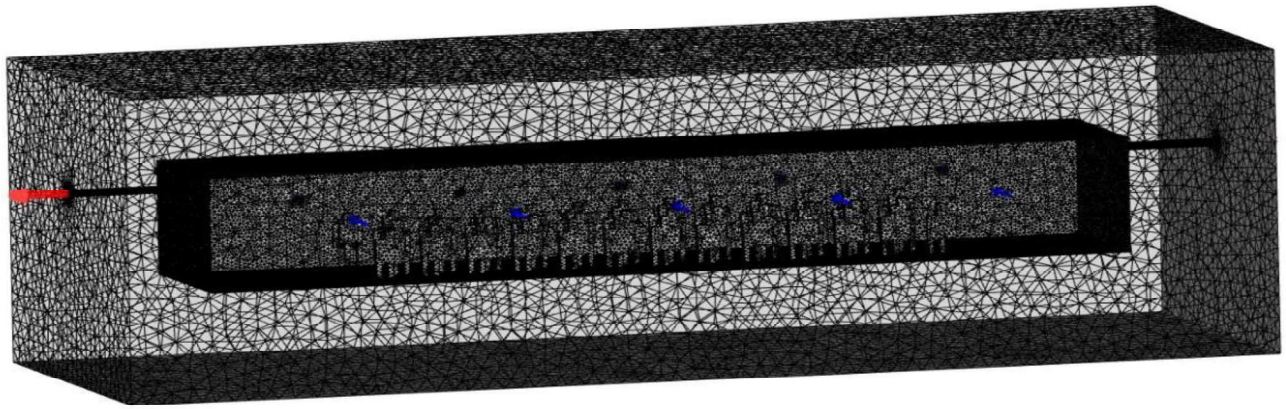

Fig. 7. Meshing of the selected MRC numerical model.

2.3.2 Initial and boundary conditions

For a MRC under the condition of MCA ventilation, the temperature control characteristics mainly depend on static parameters including the size of the MRC and the thermal conductivity, density and specific heat capacity of the surrounding rock, etc., as well as dynamic parameters including ISRT, HT, VR and VT, etc., but almost independent of the initial ambient temperature. MRCs are usually constructed in sandstone, it has been confirmed that the influence of the thermal conductivity, density, and specific heat capacity of the surrounding rock is independent to other parameters. Therefore, considering the temperature control method proposed for high temperature MRC, the current work mainly investigates the influence of dynamic parameters. The values of dynamic parameters are shown in Table 1.

Table 1. Dynamic parameters in the CFD simulations.

Dynamic parameters	Units	Reference value
ISRT (T_{isrt})	°C	25, 26, 28, 30, 32, 34
VR (G)	m^3/h	600, 750, 900, 1050, 1200, 1350, 1500
VT (T_v)	°C	16, 18, 20, 22, 24
HR from occupants (Q)	kW	5, 5.5, 6, 6.5, 7, 7.5, 8

To analyze the dynamic heat transfer characteristics between the surrounding rock and the air in a MRC under the condition of the cooled MCA, a typical numerical case was selected to show the dynamic temperature of the surrounding rock and the indoor environment within 96 h. Referred to the common surrounding rock of MRCs, the thermal conductivity, specific heat capacity and density of the surrounding rock were 2 W/(m·K), 920 J/(kg·K) and 2400 kg/m^3, respectively. For dynamic

parameters, the ISRT was 30 °C, the HR generated by occupants was 6 kW, namely the heat flux on mannequin surfaces is 60 W/m^2. The VT was 20 °C, and the VR was 900 m^3/h (0.3 m^3/min per capita), namely, the velocity magnitude at each air inlet was 6 m/s. In the process of sensitivity analysis, the value of thermal conductivity, specific heat capacity and density of the surrounding rock were not changed and the initial ambient temperature was always consistent with the ISRT, only one dynamic parameter was changed for each case, compared with the typical numerical case.

To validate the reliability and accuracy of the proposed numerical model, a simulation case is performed refers to the experiment. In this case, to ensure that the HR is comparable to that in the above experiment, the HR of the 50 mannequins is 4.2 kW, namely the heat flux on the surfaces of mannequins is 42 W/m^2. The thermal conductivity, specific heat capacity and density of the surrounding rock were 0.81 W/(m·K), 840 J/(kg·K) and 1600 kg/m^3, respectively. The ISRT was 21.8 °C and the initial ambient temperature was 24.5 °C. The ventilation parameters, ventilation time, etc., are consistent with the above experiment process.

2.3.3 Numerical methodology

In the numerical cases, kinematic viscosity of the air ranged from 1.55×10^{-5} to 1.65×10^{-5} m^2/s; the *Re* value of air inlets ranged from 27272 to 29032. Therefore, the air flow was turbulent. In the present work, the realizable *k*-*ε* turbulent model was used, because it exhibits strong performance with indoor airflows, temperature and pressure in closed structures [55]. Enhanced wall treatment with pressure gradient effects and thermal effects was selected. Also, gravity, full buoyancy effect and viscous heating were taken into account. The Boussinesq approximation was applied for the density of air to simulate the effects of temperature differences on air flow field [56]. The governing equations, including continuity equation, momentum equation, and energy equation with Boussinesq, were given as follows [57].

$$\frac{\partial \rho}{\partial t}+\frac{\partial(\rho u_i)}{\partial x_i}=0 \tag{1}$$

$$\frac{\partial u_i}{\partial t}+\frac{\partial(u_i u_j)}{\partial x_j}=-\frac{1}{\rho}\frac{\partial P}{\partial x_i}+\frac{1}{\rho}\frac{\partial}{\partial x_j}\left[\mu\left(\frac{\partial u_i}{\partial x_j}+\frac{\partial u_j}{\partial x_i}\right)-\rho\overline{u_i' u_j'}\right]-g_i\beta(T-T_0) \tag{2}$$

$$\frac{\partial T}{\partial t}+\frac{\partial(u_j T)}{\partial x_j}=\frac{1}{\rho}\frac{\partial}{\partial x_j}\left(\frac{\lambda}{C_p}\frac{\partial T}{\partial x_j}-\rho\overline{u_i' T'}\right) \tag{3}$$

Where ρ is the air density, kg/m^3; t is the time, s; x_i and x_j are the Cartesian coordinates in the i and j directions (i, j = 1, 2 and 3 corresponding to the X, Y and Z directions respectively); u_i and u_j are the mean fluid velocities in X, Y and Z directions, m/s; u'_i and u'_j are the corresponding fluctuant velocity components in the i and j directions, m/s; P is the mean air pressure, Pa; μ is the dynamic viscosity,

Pa·s; g_i is the acceleration component of gravity in the i directions, m/s^2; β is the coefficient of thermal expansion, 1/K; T is the temperature, K; T_0 is the reference temperature, K; T' is the fluctuating temperature, K; λ is the air thermal conductivity, W/(m·K); C_p is the specific heat capacity, J/(kg·K).

The realizable k-ε model consists of the following two transport equations [58].

$$\frac{\partial}{\partial t}(\rho k)+\frac{\partial}{\partial x_j}(\rho k u_j)=\frac{\partial}{\partial x_j}\left[\left(\mu+\frac{\mu_\tau}{\sigma_k}\right)\frac{\partial k}{\partial x_j}\right]+G_b+G_k-\rho\varepsilon \tag{4}$$

$$\frac{\partial}{\partial t}(\rho \varepsilon)+\frac{\partial}{\partial x_j}(\rho \varepsilon u_j)=\frac{\partial}{\partial x_j}\left[\left(\mu+\frac{\mu_\tau}{\sigma_\varepsilon}\right)\frac{\partial \varepsilon}{\partial x_j}\right]+\rho C_1 S\varepsilon-\rho C_2\frac{\varepsilon^2}{k+\sqrt{\nu\varepsilon}}+C_{1\varepsilon}\frac{\varepsilon}{k}C_{3\varepsilon}G_b \tag{5}$$

Where k is the turbulent kinetic energy, J/kg; μ_τ is the turbulent viscosity, Pa·s; σ_k and σ_ε are the Prandt1 number; G_b is the generation of turbulence kinetic energy due to buoyancy, J/(s·m^3); G_k is the generation of turbulence kinetic energy due to the mean velocity gradients, J/(s·m^3); ε is the turbulent energy dissipation, J/(kg·s); S is the modulus of the mean rate-of-strain tensor; v is the kinematic viscosity, m^2/s; C_1, C_2, $C_{1\varepsilon}$, $C_{3\varepsilon}$ are model parameters.

All cases are calculated with the pressure-velocity coupling solver, pressure-implicit with splitting of operators (PISO) was adopted. Energy, momentum, turbulent kinetic energy, turbulent dissipation and transient formulation were discretized by second-order upwind, and pressure was discretized by standard. The convergence criterion for energy is 10^{-6}, for other items is 10^{-3}. At the beginning of the calculation, use a smaller time step of 0.1 s to increase the convergence speed. When the calculation converges, gradually increase the time step to reduce the calculation time. It was proved that in the case of calculation convergence, the numerical results were independent of the time step when it is less than 60 s.

3 Results

3.1 Variation of ambient temperature in the MRC

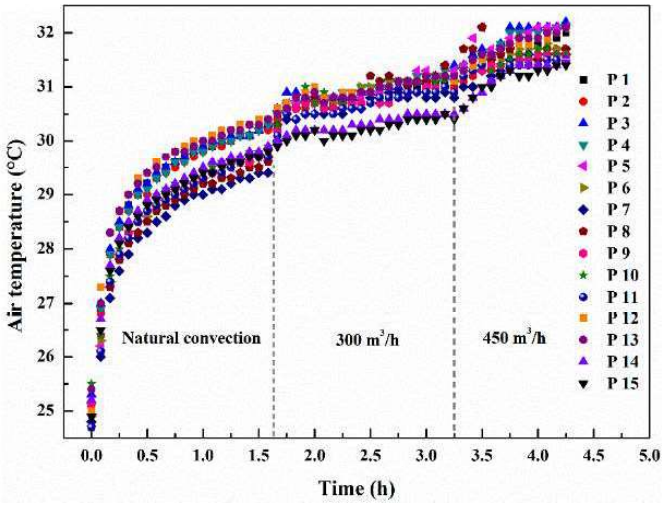

Fig. 8. Indoor ambient temperature varies with time during the experiment.

Fig. 8 plots the ambient temperature curve of measurement points over time during the experiment. It can be found that, from 0 h to 1.6 h under the condition of natural convection, the temperature of all measuring points rises rapidly from 24.5 °C to about 28.5 °C within 0.25 h, then tends to increase slowly with time. Unexpectedly, it can be found that when the MCA is sent into the MRC, the indoor ambient temperature does not decrease, but increases, and the temperature difference increases with the increase of the VR. This is attributed to the pressurized action of the compressor, which makes the air temperature greatly improved from the outdoors to the high pressure air tank. When the ventilation volume rate is 300 m^3/h and 450 m^3/h, the surface temperature of the air tank is 48 °C and 50 °C respectively, and the VT of the MCA entering the MRC is 34.7 °C and 36.2 °C, respectively. After the heat transfer process tends to be stable, the temperature of the measuring points fluctuated at 30 ~ 31℃ from 1.75 h to 3.25 h and 31 ~ 32 ℃ from 3.5 h to 4.25 h, respectively. In both cases, the indoor ambient temperature is lower than the VT, which indicates that the low-temperature surrounding rock has a strong heat absorption capacity. In addition, it can be found that every time the ventilation conditions change, a new dynamic equilibrium of the heat transfer process will reach again within less than 0.5 h.

3.2 Validation of the numerical model

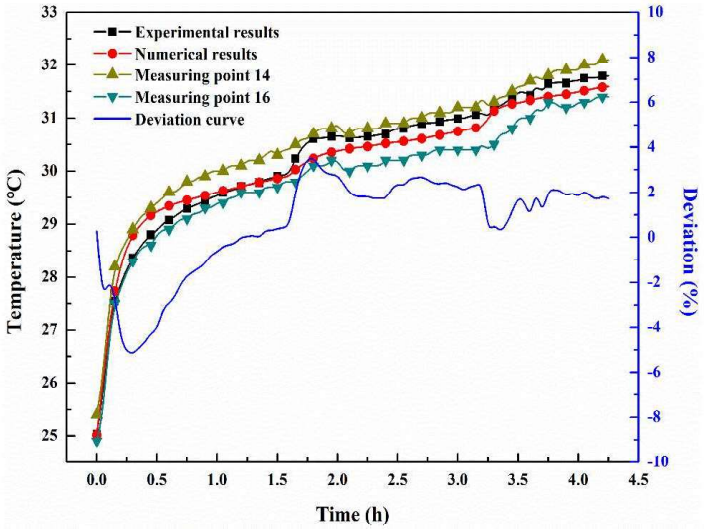

Fig. 9. Comparison of the experimental and numerical results.

Fig. 9 compares the mean ambient temperature obtained from the numerical simulation with the mean ambient temperature at the measuring point and the maximum and minimum temperatures obtained from the experiment. It can be found that under three different ventilation states, the average ambient temperature obtained by numerical simulation maintains a similar trend to the temperature of the experimental measurement points, and maintains a small temperature difference with the

experimental results. Among them, the temperature difference compared with the average value of measuring points is less than 0.3 °C, while compared with the maximum and minimum value is less than 0.6 °C. The deviation value is calculated by comparing the difference between the experimental value and the numerical value with the ISRT value, it can been found that very good agreement in both qualitatively and quantitatively is obtained, accompanying with deviation ranging from -5.2% to 3.5%, which indicates that the error caused by numerical calculation is small enough, and the selected numerical model is suitable for the current study.

3.3 Typical case analysis

To reveal the dynamic heat transfer characteristics of the indoor air and surrounding rock in a high-temperature MRC under the action of cold MCA, the numerical case with the ISRT of 30 °C, HR of 6 kW, VT of 20 °C, and VR of 900 m^3/h, was selected as the typical case.

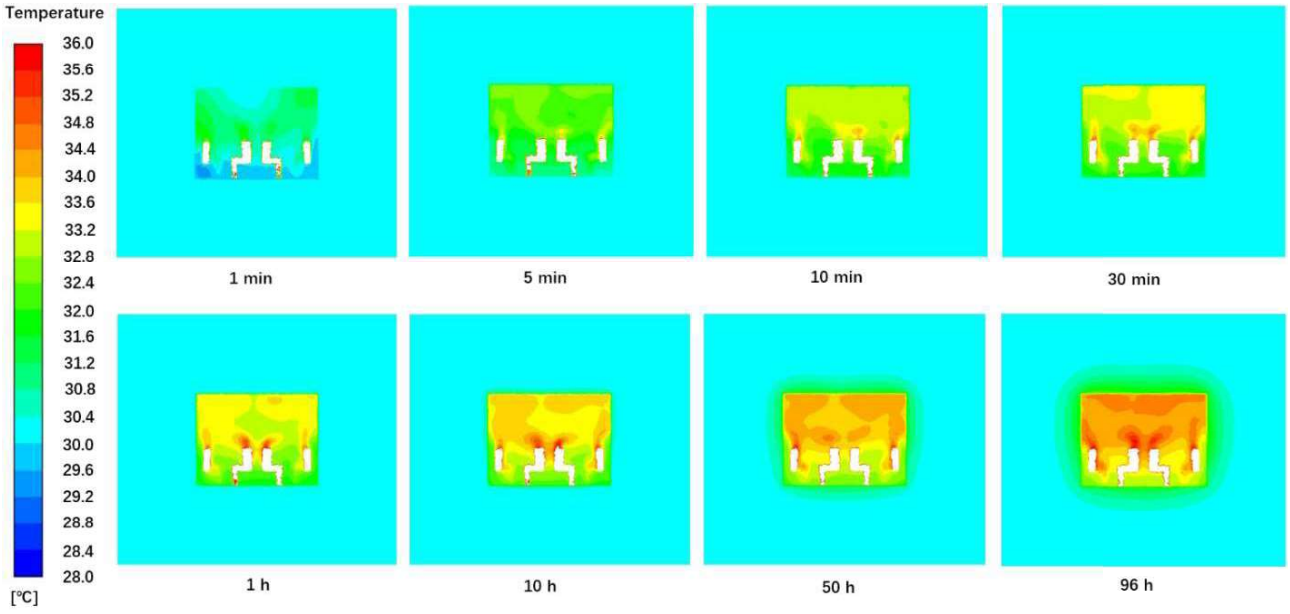

Fig. 10. Temperature distribution at different times.

Fig. 10 displays the temperature distribution on the middle-cross section of the MRC at different times. As can be seen that, due to the upward movement of hot air driven by thermal buoyancy, the ambient temperature of the space above the occupants is higher and the temperature below is lower, which makes the human activity area have relatively good thermal comfort, indicating that it is reasonable to set the fresh air inlets on both sides of the MRC above the human activity area. The indoor ambient temperature changes larger from 1 min to 30 min but smaller from 30 min to 1h. Before the ventilation lasted for 30 min, there was no significant change in the temperature near the surface of the surrounding rock. When it lasted for 50 h, the overall indoor temperature is below

34.4 °C, and the activity area was below 33.6 °C. At 96 h, the overall indoor temperature was below 34.8 °C, and the human activity area was below 34 °C.

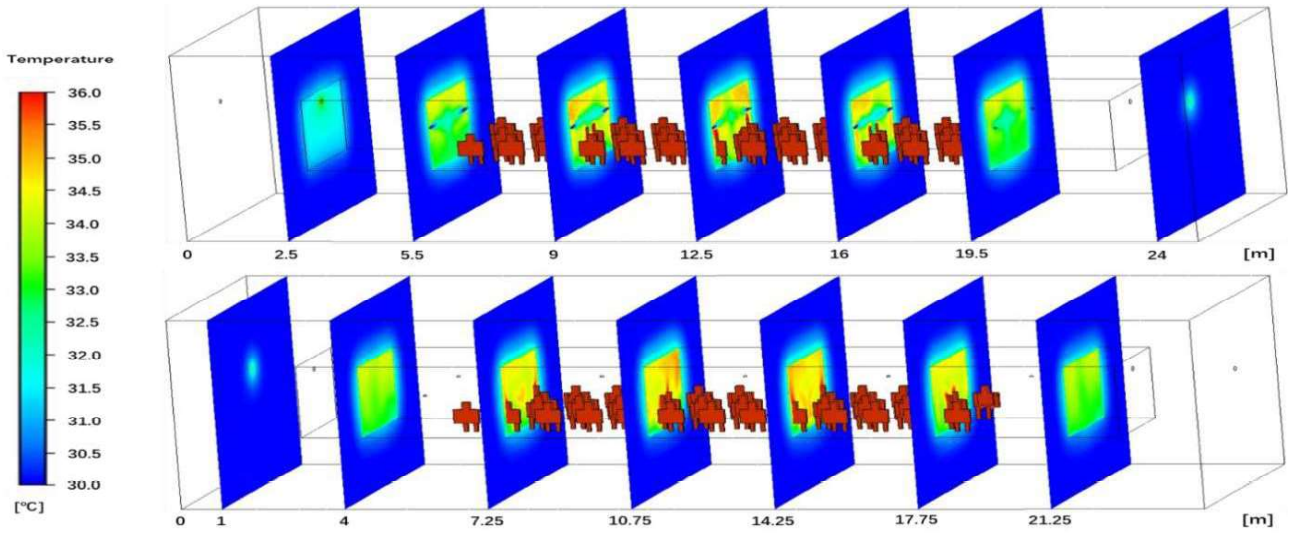

Fig. 11. Temperature distribution at 96 h.

Fig. 11 shows the temperature distribution contour on different cross-sections of the MRC at 96 h. It can be found that the ambient temperature in the jet area on the cross-section of the air inlet is relatively low, while on the cross-section of the non-air inlet, the temperature increases from bottom to top, and the ambient temperature gradually decreases from the middle to both ends. The overall indoor temperature is below 35 °C, and in the human activity area is lower than 34 °C. In addition, it can be found that the temperature of the surrounding rock has a significant change within 1 m from the wall surface, but the influence range is non-uniform around the surrounding rock. Combined with the temperature distribution in the middle-cross section at 96 h in Fig. 10. It can be observed that the heat transfer radius of the surrounding rock ranges from the largest to the smallest, in order of top, both sides and bottom.

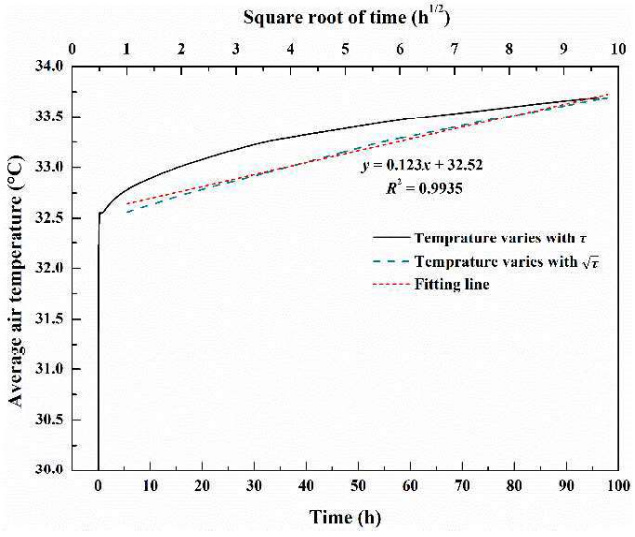

Fig. 12. Indoor air temperature varies with time.

Fig. 12 plots the curves of the indoor ambient temperature with time and the square root of time, as well as the fitted line of temperature versus the square root of time. As shown in Fig. 12, under the action of cold MCA with 20 °C, the indoor ambient temperature has experienced a short-term rapid growth, from the initial temperature of 30 °C to 32.6 °C for a period of less than 0.5 h. While the temperature growth gradient at 0.5 h slowed down significantly, the ambient temperature has only increased to 33.7 °C at 96 h, which is less than the maximum allowable temperature of 35 °C. This indicates that the ambient temperature of a high-temperature surrounding rock MRC can be effectively controlled by cooling the MCA. It can also be found from Fig. 12 that from 1 h to 96 h, the indoor ambient temperature increases approximately linearly with the square root of time, and the residual value of the linear fitting is 0.9935, which indicates that the indoor ambient temperature has a strong linear relationship with the square root of time.

3.4 Sensitivity analysis

3.4.1 Effect of ISRT

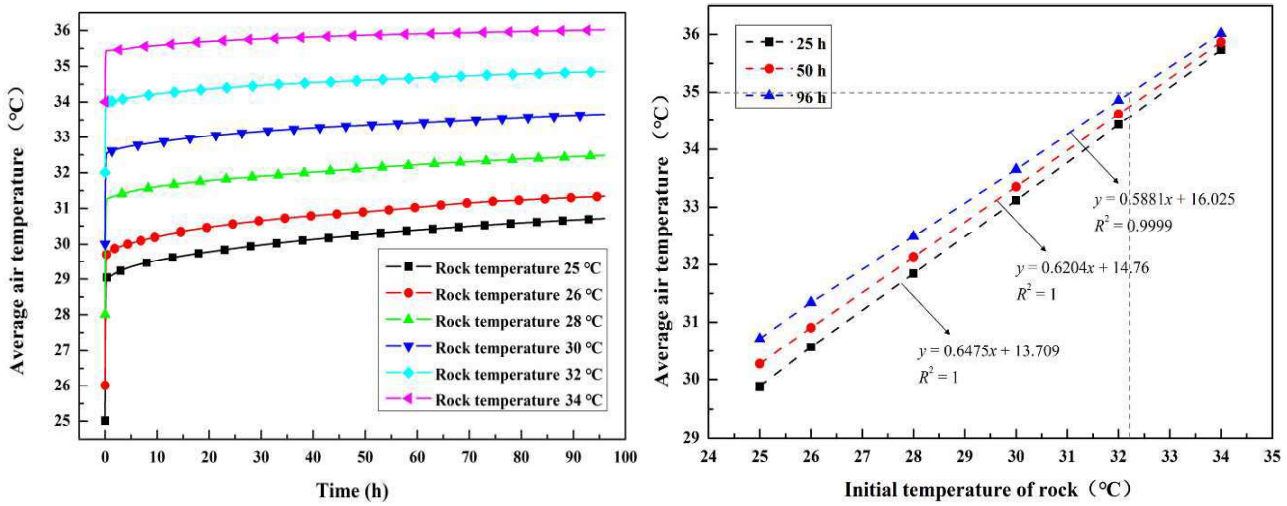

(a) Temperature varies with time (b) Temperature varies with ISRT

Fig. 13. Indoor air temperature varies with time under different ISRT.

Fig. 13 (a) and (b) respectively show the average temperature varies with time at different ISRT and the average temperature varies with ISRT at the same time. It can be observed from Fig. 13 (a) that the average air temperature increased monotonically with time when the ISRT ranged from 25 □ to 34 □. At the earlier stage, the average air temperature increases quickly in less than 0.5 h, and then enters a process of air temperature slow increase with time. As the ISRT increases, the temperature increasing trend was more moderate. In general, under the condition of MCA cooled to temperature control, the ambient temperature rising rate in the MRC decreases with the increase of the ISRT. The

reason for this is that as the ISRT increases, the temperature difference between the air and the wall tends to be great and the intensity of the convective heat transfer increases. For the case of ventilation volume rate of 0.3 m^3/min per person, the VT was 20 °C, and the average air temperature in the MRC was less than 32 °C within 96 h when the ISRT was 26 °C or below. When the ISRT reached 28 °C, the average air temperature was limited to 32.5 °C at the time of 96 h. When the ISRT reached 32 °C, the average air temperature quickly increased to 34 °C in less than 1 h, but only rises to 34.86 °C in the next 95 h, which did not exceed the allowable temperature of 35 °C. However, when the ISRT reached 34 °C, the average ambient temperature quickly exceeded 35 °C. It can be found from Fig. 13 (b) that the average air temperature in the MRC increases linearly with the ISRT, but the gradient of temperature rising gradually decreases with time. Meanwhile, it can be observed that for a MRC with an ISRT of less than 32.2 °C, the temperature control requirement of the MRC can be satisfied within 96 h when the VR is 0.3 m^3/min per person and the VT is 20 °C.

3.4.2 Effect of VT

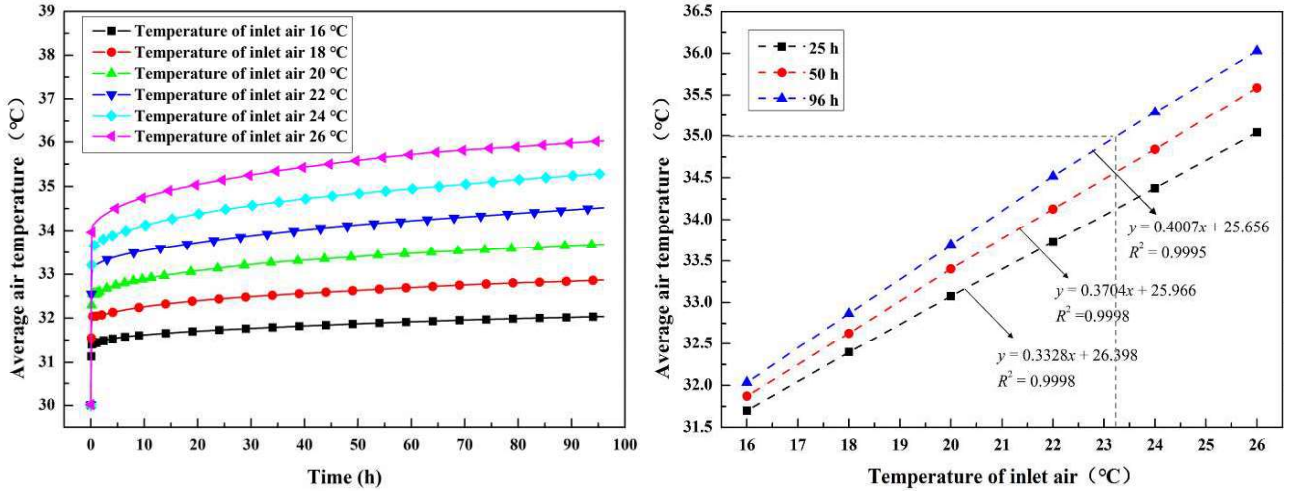

(a) Temperature varies with time (b) Temperature varies with VT

Fig. 14. Indoor air temperature varies with time under different VT.

Fig. 14 (a) and (b) show the average air temperature varies with time at different VT and the average air temperature varies with VT at the same time. It can be observed from Fig. 14 (a) that, for the MRC with an ISRT of 30 °C, the average air temperature monotonically increases with time within 96 h when the VT ranges from 16 °C to 26 °C. As the VT increases, the rising rate of the air temperature increases. The reason is that the temperature difference between the air and the wall tends to smaller with the increase of the VT, which leads to the intensity of the convective heat transfer becoming weaker. When the VT is 16 °C, the air temperature can be controlled below 32 °C within 96 h. While the VT ranges from 18 °C to 22 °C, the average air temperature will reach 32 °C quickly

but not exceed 35 °C within 96 h. When the VT is 24 °C, the average air temperature will reach 35 °C after 56 h. It can be observed from Fig. 14 (b) that the average air temperature in the MRC shows a linear upward trend with the increase of the VT, but with the increase of time, the temperature growth gradient gradually increases. Meanwhile, it can be found that, for a MRC with an ISRT of 30 °C, the temperature control requirement can be met when the ventilation volume rate is 0.3 m^3/min per person and the VT is less than 23.2 °C.

3.4.3 Effect of VR

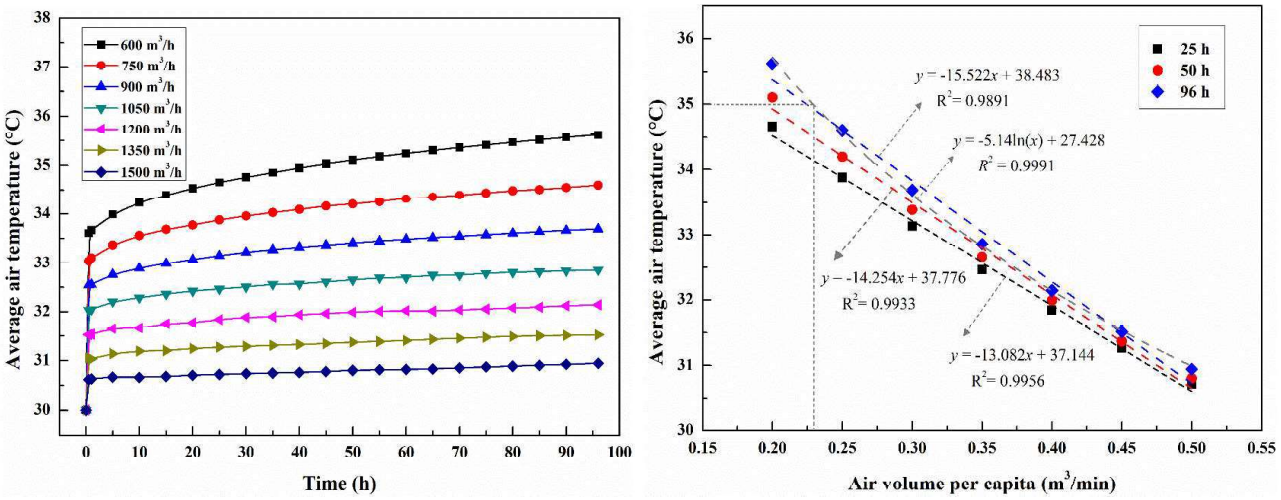

(a) Temperature varies with time (b) Temperature varies with VR

Fig. 15. Indoor air temperature varies with time under different VR.

Fig. 15 (a) and (b) represent the variation of the average temperature with time at different VRs, respectively, while the average temperature varies with the VR. It can be observed from Fig. 15 (a) that, for the MRC with an ISRT of 30 °C, when the VT is 20 °C, the average ambient temperature in the MRC generally shows an increasing trend with time, and the VR ranges from 600 to 1500 m^3/h. However, as the VR increases, the temperature growth gradient decreases. When the VR is 600 m^3/h, the average temperature reaches 35 °C at 40 h and rises to 35.62 °C at 96 h. When the VR is 750, 900, 1050, 1200 and 1350 m^3/h, the average temperature reaches 34.6, 33.7, 32.85, 32.14 and 31.57 °C at 96 h, respectively. It can be found from Fig. 15 (b), that when the ventilation lasts for 25 h and 50 h, the average air temperature shows a significant linear decrease relationship with the increase of VR. However, the linear growth relationship weakens at 96 h, and the natural logarithmic decline relationship is more significant with a residual value of 0.9991. When the per capita air supply for the MRC is more than 0.23 m^3/h, the average air temperature in the MRC can be controlled below 35 °C.

3.4.4 Effect of the HR

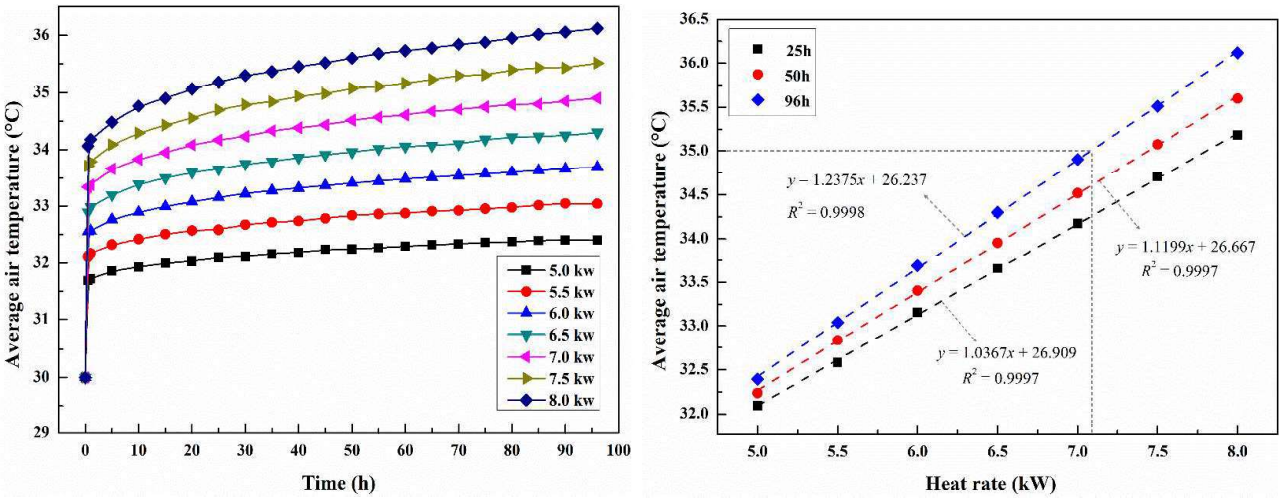

(a) Temperature varies with time (b) Temperature varies with HR

Fig. 16. Indoor air temperature varies with time under different HR.

Fig. 16 (a) and (b) show the average temperature versus time and the average temperature simultaneously versus heating rate for different heating rates, respectively. As can be seen from Fig. 16 (a), for MRC with an ISRT of 30 °C, under the condition that the VR and VT are 900 m/h and 20 °C, respectively, the average ambient temperature in the MRC generally shows a trend of increasing over time when the HR ranges from 5 to 8 kW, and the temperature growth gradient rises as the HR increases. The average air temperature rises to approximately 35 °C at 96 h when the HR is 7 kW. It can be found from Fig. 16 (b) that the average air temperature shows a significant linear increase relationship with the HR at the same time, the residual value is 0.9997, and the gradient increases as the ventilating duration increases. The average air temperature in the MRC can be controlled below 35 °C while the HR in the MRC is below 7.1 kW, approximately equivalent to the HR of 60 people.

4 Discussion

4.1 Prediction of ambient temperature in MRC

Regarding the solution of the heat transfer process of deep-buried underground buildings, the common analytical method is to simplify the cross-section of underground buildings to equivalent radius cylinders for solving [43], [44]. However, according to the above numerical results in Fig.10, the heat transfer process between the surrounding rock and the air in the MRC shows non-uniformity within 96 h. It can be known from Fig. 12, that the ambient temperature in the MRC shows a strong linear correlation with the square root of time from 1 h to 96 h. Therefore, after the ventilation lasts

more than 1 h, the relationship between the average air temperature and time in MRC can be expressed as follows

$$T_a(\tau) = K\sqrt{\tau} + L \quad (6)$$

Where, T_a is the ambient temperature in the MRC, □; τ is the ventilating time, h; K is the slope, □/h$^{1/2}$; L is the intercept, □.

For all the above numerical simulation cases, according to Eq. (6), the linear fitting formula under different working conditions can be obtained when the τ value ranges from 1 h to 96 h. The parameter settings and fitting relationship of the relevant numerical cases are shown in Table 2. Considering that the difference value between the fitting formula and the numerical data is less than 0.1 □, in particular, the difference is almost negligible when the time τ is greater than 20 h, as shown in Fig. 12, so the error band of fitting formulas are not mentioned in Table 2.

Table 2. Parameter settings and fitting relationship of the numerical cases.

T_{isrt} (℃)	T_v (℃)	G (m^3/h)	Q (kW)	Fitting formula	R^2	K	L
25	20	900	6	$y = 0.1829x + 28.963$	0.9981	0.1829	28.963
26	20	900	6	$y = 0.1765x + 29.661$	0.998	0.1765	29.661
28	20	900	6	$y = 0.145x + 31.172$	0.9994	0.145	31.172
30	20	900	6	y = 0.123x + 32.52	0.9935	0.123	32.52
32	20	900	6	$y = 0.0968x + 33.926$	0.9982	0.0968	33.926
34	20	900	6	$y = 0.0662x + 35.39$	0.9928	0.0662	35.39
30	16	900	6	$y = 0.0665x + 31.399$	0.9988	0.0665	31.399
30	18	900	6	$y = 0.0951x + 31.956$	0.998	0.0951	31.956
30	22	900	6	$y = 0.147x + 33.08$	0.9997	0.147	33.08
30	24	900	6	$y = 0.1795x + 33.556$	0.9984	0.1795	33.556
30	26	900	6	$y = 0.2001x + 34.135$	0.9935	0.2001	34.135
30	20	600	6	y = 0.2156x + 33.554	0.9967	0.2156	33.554
30	20	750	6	y = 0.1621x + 33.042	0.996	0.1621	33.042
30	20	1050	6	y = 0.0882x + 32.022	0.9902	0.0882	32.022
30	20	1200	6	y = 0.0678x + 31.485	0.9874	0.0678	31.485
30	20	1350	6	y = 0.0531x + 31	0.9932	0.0531	31
30	20	1500	6	y = 0.0358x + 30.558	0.9501	0.0358	30.558
30	20	900	5	y = 0.0772x + 31.69	0.9948	0.0772	31.69
30	20	900	5.5	y = 0.1002x + 32.103	0.995	0.1002	32.103
30	20	900	6.5	y = 0.1488x + 32.886	0.9943	0.1488	32.886
30	20	900	7	y = 0.1677x + 33.304	0.993	0.1677	33.304
30	20	900	7.5	y = 0.1936x + 33.68	0.9927	0.1936	33.68
30	20	900	8	y = 0.2122x + 34.076	0.9943	0.2122	34.076

Fig. 17 (a) to (d) plot the variation of the values of K and L with four dynamic factors, namely ISRT, VT, VR, and HR, respectively. It can be found that the K value shows a strong linear relationship with the VT, HR and ISRT following with $R^2 > 0.99$, and has a good logarithmic

relationship with the VR following with R^2 close to 0.99. The B value shows a strong linear relationship with the four factors following with R^2 close to 1, decreasing with the ISRT and VR, but increasing with the VT and HR.

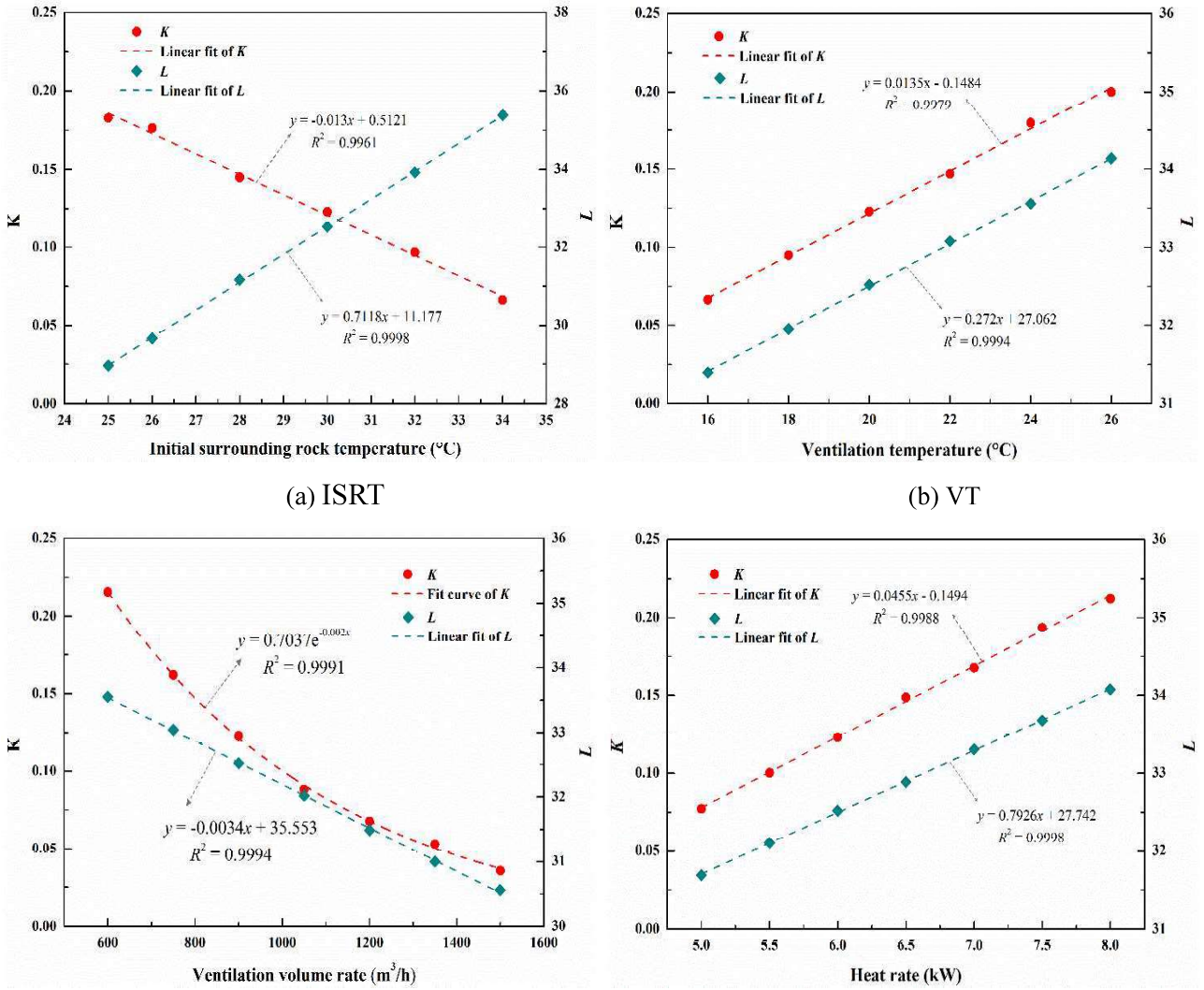

(a) ISRT (b) VT

(c) VR (d) HR

Fig. 17 Value of K and L vary with dynamic influencing factors.

Therefore, the mathematical relationship of K, L with the four factors can be respectively assumed as follows

$$K = f(T_v, T_{isrt}, G, Q) = hT_v + iT_{isrt} + je^{lG} + mQ + n \quad (7)$$

$$L = F(T_v, T_{isrt}, G, Q) = aT_v + bT_{isrt} + cG + dQ + f \quad (8)$$

Where, T_v is the VT, □; T_{isrt} is the ISRT, □; G is the VR, m^3/h; Q is the HR generated by occupants, kW; h, i, j, l, m and n are coefficients in K expression; a, b, c, d and f are coefficients in L expression.

Bring the different parameter values and the corresponding values of K and L in Table 1 into Eqs. (7) and (8), respectively, through regression analysis, in the case of 95% confidence intervals, solve the trusted values of the coefficients h, i, j, etc., respectively. Then the mathematical relationships of

K and L are as follows

$$K = f(T_v, T_{isrt}, G, Q) = (1.353T_v - 1.301T_{isrt} + 4.628Q) \times 10^{-2} + 0.7e^{-0.002G} - 0.155 \quad (9)$$

$$L = F(T_v, T_{isrt}, G, Q) = 0.271T_v + 0.711T_{isrt} - 3.339 \times 10^{-3}G + 0.786Q + 4.069 \quad (10)$$

According to Eqs. (6), (9) and (10), under the condition of cooled MCA, the average air temperature in the MRC after 1 h of ventilation can be calculated as follows

$$T_a(\tau) = [(1.353T_v - 1.301T_{isrt} + 4.628Q) \times 10^{-2} + 0.7e^{-0.002G} - 0.155]\sqrt{\tau} + 0.271T_v + 0.711T_{isrt} - 3.339 \times 10^{-3}G + 0.786Q + 4.069 \quad (11)$$

The proposed method of Eq. (11) will help to determine whether the condition of the MCA cooling temperature control meets the room temperature control of the MRC. Also, it can provide theoretical guidance for the design of air temperature control system in a MRC. However, it should be noted that: firstly, the Eq. (11) is limited to a ventilating MRC within 1 ~ 96 h; secondly, the Eq. (11) does not consider the influence of rock thermal properties and the geometric structure of the MRC. When facing different types of rocks and different structures, further corrections are required.

4.2 Requirements for MCA cooling devices

According to Eq. (11), the relationship between the VR and VT of MCA cooling device for a high-temperature MRC is as follows

$$(0.01353\sqrt{\tau} + 0.271)T_v + 0.7e^{-0.002G}\sqrt{\tau} - 3.339 \times 10^{-3}G = (0.01301\sqrt{\tau} - 0.711)T_{isrt} - (0.786 + 0.04628\sqrt{\tau})Q + T_a(\tau) - 4.069 + 0.155\sqrt{\tau} \quad (12)$$

In order to make the ambient temperature in the MRC not exceed the allowable temperature (T_{allowed}) within 96 h, according to Eq. (12), the relationship between the VR and VT should meet the requirements of the following formula

$$T_v + 16.9952e^{-0.002G} - 8.2739 \times 10^{-3}G \le 2.4779T_{\text{allowed}} - 1.446T_{isrt} - 3.0713Q - 6.3196 \quad (13)$$

Assuming that the values of the VR and VT are constant, and the target temperature set at 96 h is T_{goal}, thus, the relationship between the VR and VT is as follows

$$T_v = 2.4779T_{\text{goal}} + 8.2739 \times 10^{-3}G - 16.9952e^{-0.002G} - 1.446T_{isrt} - 3.0713Q - 6.3196 \quad (14)$$

Thus, the cooling storage capacity of MCA cooling devices that meets the temperature control needs of the MRC for occupants within 96 h can be calculated as follows

$$Q_{\text{cool}} = \rho C_p G(T_{\text{MCA}} - T_v)\tau = 96\rho C_p G(T_{\text{MCA}} - T_v) \quad (15)$$

where, Q_{cool} is the cool capacity, T_{MCA} is the temperature of the original MCA.

5 Conclusions

In this work, a temperature control system by cooling MCA was proposed for MRCs with high ISRT. An experiments was conducted to test the temperature control characteristics of the MRC under

the MCA. Moreover, a MRC numerical model was established and validated, the effects of dynamic factors such as ISRT, HR, VR and VT on the temperature control characteristics of the MRC under cooled MCA were analyzed. The following specific conclusions can be drawn:

(1) The heat transfer process between the rock wall and the air will reach a dynamic equilibrium within 0.5 h under a disturbance action in the MRC, and the low-temperature surrounding rock has a strong heat absorption ability.

(2) Under the action of cooled MC, the ambient temperature of the MRC increases linearly with the square root of the time from 1 h to 96 h, the temperature gradient increases linearly with the VT and HR, but decreases linearly with the ISRT, and decreases exponentially with the VR.

(3) In the case of a VR of 0.3 m^3/min per person, when the VT is 20 °C, the ambient temperature in a MRC with an ISRT of 32 °C or below can be controlled to less than 35 °C, the VT should be below 23.2 ° C to meet the temperature control requirements of a MRC with an ISRT of 30 °C.

(4) An empirical correlation is proposed to predict the ambient temperature of an MCA under cooled MCA. On this basis, the calculation method of VT and cool storage capacity that meet the temperature control of the MCA under a specific VR is derived.

This work provides a basis for the temperature prediction, transient heat load, and the cooling capacity for the high-temperature MRC using the pressure-air-ice storage coupling method to control the temperature. Future work, could involve the development of the ice storage device for cooling MCA and the experiment in engineering applications.

Acknowledgments

The authors would like to thank the financial support from the National Natural Science Foundation of China (NO. 52168013 and NO. 51908080), the Guizhou Provincial Science and Technology Projects (No. ZK[2022]151 and No. [2020]2004) and the State Key Laboratory of Gas Disaster Detecting, Preventing and Emergency Controlling Open-fund Project (No.2021SKLKF10).

References

[1] Z. Fareed, U. Pata. Renewable, non-renewable energy consumption and income in top ten renewable energy-consuming countries: Advanced Fourier based panel data approaches. Renewable Energy 194 (2022), 805-821. https://doi.org/10.1016/j.renene.2022.05.156

[2] L. Zhao, Z. Liu, L. Cheng. How will China's coal industry develop in the future? A quantitative analysis with policy implications. Energy 235 (2021), 121406. https://doi.org/10.1016/j.energy.2021.121406

[3] A. Singh, A. Kumar. Ecological performances of exotic and native woody species on coal mine spoil in Indian dry tropical region. Ecological Engineering 174 (2022), 106470. https://doi.org/10.1016/j.ecoleng.2021.106470

[4] K. Wang, J. Zhang, B. Cai, S. Yu. Emission factors of fugitive methane from underground coal mines in China: Estimation and uncertainty. Applied Energy 250 (2019), 273-282. https://doi.org/10.1016/j.apenergy.2019.05.024

[5] P. Knights, B. Scanlan. A study of mining fatalities and coal price variation. International Journal of Mining Science and Technology 29 (2019), 599-602. https://doi.org/10.1016/j.ijmst.2019.06.016

[6] J. Zhang, D. Cliff, K. Xua, G. You. Focusing on the patterns and characteristics of extraordinarily severe gas explosion accidents in Chinese coal mines. Process Safety and Environmental Protection 117 (2018), 390-398. https://doi.org/10.1016/j.psep.2018.05.002

[7] Y. Zhu, D. Wang, Z. Shao, C. Xu, X. Zhu, X. Qi, F. Liu. A statistical analysis of coalmine fires and explosions in China. Process Safety and Environmental Protection 121 (2019), 357-366. https://doi.org/10.1016/j.psep.2018.11.013

[8] K. Margolis, C. Westerman, K. Kowalski-Trakofler. Underground mine refuge chamber expectations training: program development and evaluation. Safety Science 49 (2011), 522–530. https://doi.org/10.1016/j.ssci.2010.12.008

[9] K. Karadeniz, S. Nowak, D. Guner, et al. Evaluation on underground refuge alternatives and explosion survivability: a review. Mining, Metallurgy & Exploration 39 (2022), 2311-2331. https://doi.org/10.1007/s42461-022-00682-1

[10] R. Lotfian, M. Najafi. Optimal location of emergency stations in underground mine networks using a multiobjective mathematical model. Injury Prevention Journal of the International Society for Child & Adolescent Injury Prevention 25 (2019), 264-272. http://dx.doi.org/10.1136/injuryprev-2017-042657

[11] Z. Shao, Y. Yang, M. Kumral . Optimal refuge chamber position in underground mines based on tree network. International Journal of Injury Control and Safety Promotion 1 (2023), 1-16. https://doi.org/10.1080/17457300.2022.2164311

[12] A. Jha, A. Verburg, P. Tukkaraja. Internet of Things-Based Command Center to Improve Emergency Response in Underground Mines. Safety and Health at Work 13 (2022), 40-50. https://doi.org/10.1016/j.shaw.2021.10.003

[13] K. Greene. Notes from the Particle Physics Underground, 2015, 08. https://newscenter.lbl.gov/2015/08/03/notes-from-the-particle-physics-underground/

[14] MineArc. 200-person permanent refuge chamber to Indonesian mine. 2014. https://minearc.com/200-person-permanent-refuge-chamber/

[15] M. Paul, D. Iryanto, D. Quinn, A. Widyastutie, A. Mone. Design and construction of high capacity fixed refuge

chambers at PT freeport Indonesia's underground operations. Proceedings of the 11th International Mine Ventilation Congress. Springer, Singapore 2019. https://doi.org/10.1007/978-981-13-1420-9_73

[16] C. Ashley, R. Lopez, X. Garzon-Villalba, T. Bernard. Thermal exposure limit in a simulated refuge alternative. Mining, Metallurgy & Exploration 37 (2020), 179-186. https://doi.org/10.1007/s42461-019-00134-3

[17] T. Bernard, D. Yantek, E. Thimons. Estimation of metabolic heat input for refuge alternative thermal testing and simulation. Mining Engineering 70 (2018), 50-54. https://doi.org/10.19150/me.8429

[18] Z. Zhang, T. Jin, H. Wu, R. Day, X. Gao, K. Wang, R. Mao. Experimental investigation on environmental control of a 50-person mine refuge chamber. Building and Environment 210 (2022), 108667. https://doi.org/10.1016/j.buildenv.2021.108667

[19] D. Yantek, L. Yan, N. Damiano, M. Reyes, J. Srednicki. A test method for evaluating the thermal environment of underground coal mine refuge alternatives. International Journal of Mining Science and Technology 29 (2019), 343-355. https://doi.org/10.1016/j.ijmst.2019.01.004

[20] D. Yantek, L. Yan, P. Bissert, M. Klein. Effects of mine strata thermal behavior and mine initial temperatures on mobile refuge alternative temperature. Mining Engineering 69 (2017), 41-48. https://10.19150/me.7393

[21] L. Yan, D. Yantek, M. Reyes. Underground mine air and strata temperature change due to the use of refuge alternatives. Mining, Metallurgy & Exploration 37 (2020), 773-781. https://doi.org/10.1007/s42461-019-00153-0

[22] Z. Zhang, R. Day, K. Wang, H. Wu, Y. Yuan. Thermal performance analysis of an underground closed chamber with human body heat sources under natural convection. Applied Thermal Engineering 145 (2018), 453-463. https://doi.org/10.1016/j.applthermaleng.2018.09.068

[23] Z. Zhang, H. Wu, K. Wang, R. Day, Y. Yuan. Thermal performance of a mine refuge chamber with human body heat sources under ventilation. Applied Thermal Engineering 8 (2019), 114243. https://doi.org/10.1016/j.applthermaleng.2019.114243

[24] L. Yan, D. Yantek. Portable refuge alternatives temperature and humidity tests. Mining Engineering 70 (2018), 43-49. https://doi.org/10.19150/me.8546

[25] Y. Yuan, X. Gao, H. Wu, Z. Zhang, X. Cao, L. Sun, N. Yu. Coupled cooling method and application of latent heat thermal energy storage combined with pre-cooling of envelope: method and model development. Energy 119 (2017), 817-833. https://doi.org/10.1016/j.energy.2016.11.058

[26] Y. Li, Y. Yuan, C. Li, X. Han, X. Zhang. Human responses to high air temperature, relative humidity and carbon dioxide concentration in underground refuge chamber. Building and Environment 131 (2018), 53-62. https://doi.org/10.1016/j.buildenv.2017.12.038

[27] B. Yang, H. Yao, P. Yang, Y. Guo, F. Wang, C. Yang, A. Li. Che. Effects of thermal and acoustic environments

on workers' psychological and physiological stress in deep underground spaces. Building and Environment 212 (2022), 108830. https://doi.org/10.1016/j.buildenv.2022.108830

[28] R. Qiao, X. Li, S. Gao, X. Ma. Improvement of thermal comfort for underground space: Data enhancement using variational autoencoder. Building and Environment 207 (2022), 108457. https://doi.org/10.1016/j.buildenv.2021.108457

[29] K. Zhong, Q. Meng, X. Liu. A ventilation experimental study of thermal performance of an urban underground pipe rack. Energy and Buildings 241 (2021), 110852. https://doi.org/10.1016/j.enbuild.2021.110852

[30] M. Vaccarini, A. Giretti, L. Tolve, M. Casals. Model predictive energy control of ventilation for underground stations. Energy and Buildings 116 (2016), 326-340. https://doi.org/10.1016/j.enbuild.2016.01.020

[31] J. Trackemas, E. Thimons, E. Bauer, M. Sapko. Facilitating the use of built-in-place refuge alternatives in mines. USA, DHHS (NIOSH) publication No. RI9698, Pittsburgh, PA. 2015. https://www.cdc.gov/niosh/mining/UserFiles/works/pdfs/2015-114.pdf

[32] Z. Zhang, H. Wu, K. Wang, R. Day, Y. Yuan. Air quality control in mine refuge chamber with ventilation through pressure air Pipeline. Process Safety and Environmental Protection 135 (2020), 46-58. https://doi.org/10.1016/j.psep.2019.12.014

[33] H. Shao, S. Jiang, W. Tao, Z. Wu, W. Zhang, K. Wang. Theoretical and numerical simulation of critical gas supply of refuge chamber. International Journal of Mining Science and Technology 26 (2016), 389-393. http://dx.doi.org/10.1016/j.ijmst.2016.02.004

[34] B. Friedenstein, C. Cilliers, J. Rensburg. Simulating operational improvements on mine compressed air systems. South African Journal of Industrial Engineering 29 (2018), 68-80. http://dx.doi.org/10.7166/29-3-2049

[35] A. Halim, J. Brune. Do refuge chambers represent a good strategy to manage emergencies in underground coal mines?. Mining, Metallurgy & Exploration 36 (2019), 1191-1199. https://doi.org/10.1007/s42461-019-0100-8

[36] S. Wang, L. Jin, Z. Han, Y. Li, S. Ou, N. Gao, Z. Huang. Discharging performance of a forced-circulation ice thermal storage system for a permanent refuge chamber in an underground mine. Applied Thermal Engineering 110 (2017), 703-709. https://doi.org/10.1016/j.applthermaleng.2016.08.192

[37] Y. Du, W. Gai, L. Jin, W. Sheng. Thermal comfort model analysis and optimization performance evaluation of a multifunctional ice storage air conditioning system in a confined mine refuge chamber. Energy 141 (2017), 964-974. https://doi.org/10.1016/j.energy.2017.09.123

[38] X. Xu, S. You, X. Zheng, H. Zhang, S. Liu. Cooling performance of encapsulated ice plates used for the underground refuge chamber. Applied Thermal Engineering 112 (2017), 259-272.

https://doi.org/10.1016/j.applthermaleng.2016.10.072

[39] Y. Jia, Y. Liu, S. Sun, H. Li, L. Jiao. Refrigerating characteristics of ice storage capsule for temperature control of coal mine refuge chamber. Applied Thermal Engineering 75 (2015), 756-762. https://doi.org/10.1016/j.applthermaleng.2014.10.036

[40] J. Yang, L. Yang, J. Wei, Y. Ma, Z. Zhang. Study on open-cycle carbon dioxide refrigerator for movable mine refuge chamber. Applied Thermal Engineering 52 (2013), 304-312. https://doi.org/10.1016/j.applthermaleng.2012.12.014

[41] X. Gao, Y. Yuan, X. Cao, H. Wu, X. Zhao. Coupled cooling method and application of latent heat thermal energy storage combined with pre-cooling of envelope: Sensitivity analysis and optimization. Process Safety and Environmental Protection 107 (2017), 438-453. https://doi.org/10.1016/j.psep.2017.03.005

[42] X. Gao, Y. Yuan, X. Cao, H. Wu, X. Zhao. Coupled cooling method and application of latent heat thermal energy storage combined with pre-cooling of envelope: Optimization of pre-cooling with intermittent mode. Sustainable Cities and Society 38 (2018), 370-381. https://doi.org/10.1016/j.scs.2018.01.014

[43] X. Gao, Y. Yuan, X. Cao, H. Wu, X. Zhao, D. Yan. Coupled cooling method and application of latent heat thermal energy storage combined with pre-cooling of envelope: Temperature control using phase-change chair. Sustainable Cities and Society 42 (2018), 38-51. https://doi.org/10.1016/j.scs.2018.06.032

[44] X. Gao, Z. Zhang, Y. Yuan, X. Cao, C. Zeng, D. Yan. Coupled cooling method for multiple latent heat thermal storage devices combined with pre-cooling of envelope: Model development and operation optimization. Energy 159 (2018), 508-524. https://doi.org/10.1016/j.energy.2018.06.151

[45] L. Yan, D. Yantek, M. Reyes, B. Whisner, J. Bickson, J. Srednicki, N. Damiano, E. Bauer. Cryogenic air supply for cooling built-in-place refuge alternatives in hot mine. Mining, Metallurgy & Exploration 37 (2020), 861-871. https://doi.org/10.1007/s42461-020-00194-w

[46] L. Yan, D. Yantek, T. Lutz, J. Yonkey, J. Srednicki. Underground Mine Refuge Alternatives Heat Mitigation. Journal of Thermal Science and Engineering Applications: Transactions of the ASME 12 (2020), 021019. https://doi.org/10.1115/1.4044345

[47] X. Gao, Z. Zhang, Y. Xiao. Modelling and thermo-hygrometric performance study of an underground chamber with a long vertical earth-air heat exchanger system. Applied Thermal Engineering 180 (2020), 115773. https://doi.org/10.1016/j.applthermaleng.2020.115773

[48] X. Gao, Y. Xiao, P. Gao. Thermal potential improvement of an earth-air heat exchanger (EAHE) by employing backfilling for deep underground emergency ventilation. Energy 250 (2022), 123783. https://doi.org/10.1016/j.energy.2022.123783

[49] H. Mao, X. Gao, Y. Liu, J. Lin, Y. Xiao. Fast calculation model for heat and mass transfer in a deep-buried underground air tunnel using Z-transfer coefficient method. Energy and Buildings 247 (2021), 111139. https://doi.org/10.1016/j.enbuild.2021.111139

[50] J. Guo, A. Li, C. Zhang, J. Li, J. Che, J. Xiong, X. Jiao. Modeling effective heat transfer and ventilation in deeply buried underground tunnels. International Journal of Thermal Sciences 184 (2023), 107949. https://doi.org/10.1016/j.ijthermalsci.2022.107949

[51] L. Chen, J. Li, Y. Zhang, F. Han, C. Ji, J. Zhang. Study on coupled heat transfer and seepage in large sparsely fractured surrounding rocks in deep underground spaces. Applied Thermal Engineering 162 (2019), 114277. https://doi.org/10.1016/j.applthermaleng.2019.114277

[52] J. Yang, S. Ni, W. Weng. Modelling heat transfer and physiological responses of unclothed human body in hot environment by coupling CFD simulation with thermal model. International Journal of Thermal Sciences 120 (2017), 437-445. https://doi.org/10.1016/j.ijthermalsci.2017.06.028

[53] Y. Xu, Z. Li, J. Wang, Y. Chen, R. Li, Q. Wang, M. Ji. Ventilation and heat exchange characteristics in high geotemperature tunnels considering buoyancy-driven flow and groundwater flow. International Journal of Thermal Sciences 173 (2022), 107400. https://doi.org/10.1016/j.ijthermalsci.2021.107400

[54] W. Huo, Y. Cheng, Y. Jia, C. Guo. Research on the thermal comfort of passenger compartment based on the PMV/PPD. International Journal of Thermal Sciences 184 (2023), 107876. https://doi.org/10.1016/j.ijthermalsci.2022.107876

[55] Q. Cao, M. Liu, X. Li, C. Lin, D. Wei, S. Ji, T. Zhang, Q. Chen. Influencing factors in the simulation of airflow and particle transportation in aircraft cabins by CFD. Building and Environment 207 (2021), 108413. https://doi.org/10.1016/j.buildenv.2021.108413

[56] J. Lin, Y. Kong, L. Zhong. Optimization of environment control system for narrow sleeping space in underground shelters. Energy and Buildings 263 (2022), 112043. https://doi.org/10.1016/j.enbuild.2022.112043

[57] T. Wu, C. Lei. On numerical modelling of conjugate turbulent natural convection and radiation in a differentially heated cavity. International Journal of Heat and Mass Transfer 91 (2015), 454-466. https://doi.org/10.1016/j.ijheatmasstransfer.2015.07.113

[58] M. Boulet, B. Marcos, M. Dostie, C. Moresoli, CFD modeling of heat transfer and flow field in a bakery pilot oven. Journal of Food Engineering 97 (2010), 393-402. https://doi.org/10.1016/j.jfoodeng.2009.10.034